Mathematical Modelling and Analysis
Volume 15 Number 4, 2010, pages 409–430
Doi:10.3846/1392-6292.2010.15.409-430

ISSN 1392-6292 print
ISSN 1648-3510 online
www.vgtu.lt/mma/

Effective Numerical Integration of Traveling Wave Model for Edge-Emitting Broad-Area Semiconductor Lasers and Amplifiers

R. Čiegis[1] **and M. Radziunas**[2]

[1] *Vilnius Gediminas Technical University*
Saulėtekio al. 11, LT–10223, Vilnius, Lithuania
E-mail: rc@fm.vgtu.lt

[2] *Weierstrass Institute for Applied Analysis and Stochastics*
Mohrenstarsse 39, 10117 Berlin, Germany
E-mail: radziunas@wias-berlin.de

Received September 11, 2010; published online November 15, 2010

Abstract. We consider a system of $1+2$ dimensional partial differential equations which describes dynamics of edge-emitting broad area semiconductor lasers and amplifiers. The given problem is defined on the unbounded domain. After truncating this domain and defining an auxiliary $1+1$ dimensional linear Schrödinger problem supplemented with different artificial boundary conditions, we propose an effective strategy allowing to get a solution of the full problem with a satisfactory precision in a reasonable time. For further speed up of the numerical integration, we develop a parallel version of the algorithm.

Keywords: transparent boundary conditions, finite-difference method, Crank–Nicolson scheme, error estimate, traveling wave model, parallel algorithms, broad area lasers, semiconductor laser.

AMS Subject Classification: 65N06; 65N12; 65Z05.

1 Introduction

High power high brightness edge-emitting semiconductor lasers and optical amplifiers are compact devices and they can serve a key role in different laser technologies such as free space communication [4], optical frequency conversion [10], printing, marking materials processing [12], or pumping fiber amplifiers [11].

To simulate the generation and/or propagation of the optical fields along the cavity of the considered device we use a 2+1 dimensional system of PDEs, this system is based on the traveling wave (TW) equations for slowly varying in

time longitudinally counter-propagating and laterally diffracted optical fields [2, 13].

The precise dynamic simulations of long and broad or tapered devices and tuning/optimization of the model with respect to one or several parameters, require huge CPU time and memory resources. Due to a considerable length of several millimeters and width of several hundreds of micrometers for high power semiconductor lasers we obtain a large system of discrete nonlinear equations with several million of spatial variables. For example, a rather sparse discretization of the computational domain for a 4 mm long and ~ 0.25 mm broad device containing a narrow ~ 3 μm waveguide part (see Ref. [13] and Fig. 1) is discretized by using $\sim 0.5 \cdot 10^6$ grid points, thus we have to find $\sim 4.5 \cdot 10^6$ real variables within each time integration step. The simulation of a laser during typical 3 ns transient time which, usually, is just enough to simulate the switching on of the laser or the relaxation of the device towards some new attractor after a change of parameters requires $\sim 0.5 \cdot 10^5$ time iterations and can be performed on a single processor computer in, approximately, 4-5 hours [13].

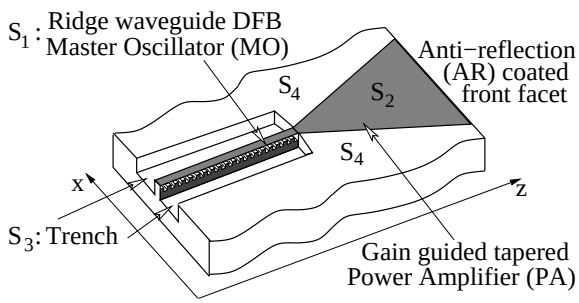

Figure 1. Schematic view of DFB tapered MOPA. S_1–S_4 denote four parts of the device.

Some speed-up of computations can be achieved by using problem-dependent relations of the grid steps, including also variable steps in lateral direction of the device [7, 9]. All these grid optimizations, however, are not sufficient once one- or a few- parameter studies should be performed (they can correspond to simulation times $\sim$1000 ns) The required results can only be computed in acceptable time by using parallel computers and parallel solvers.

In this paper we present a mathematical model and a parallel simulation technique suitable for fast long time dynamical computation of high power broad area semiconductor lasers. Seeking to optimize the performance of the numerical schemes for TW model discussed earlier in [7, 9] we investigate here also a related 1+1 dimensional Schrödinger equation describing a diffractive beam propagation in linear gain or/and index guided media. The results obtained in solving this simplified auxiliary problem by using artificial boundary conditions [1, 14] and special non-uniform space grids with discretization steps from the moderate-to-large sizes let us to choose a proper strategy allowing to resolve the full TW model with a required precision in reasonable time.

2 Traveling-Wave Model for Broad Area Lasers

The TW model equations will be considered in the dimensionless unbounded region $Q = \{(z,x,t) : (z,x,t) \in Q_{z,x} \times (0,T]\}$, where $Q_{z,x} = \{(z,x) : (z,x) \in (0,L) \times \mathbb{R}\}$ is a spatial domain, L represents the length of the laser, x is the coordinate of the unbounded lateral axis of the device, and T defines the length of the time interval where we perform integration. (z,x,t) are dimensionless spatial coordinates and time, scaled by

$$z_0 = 10^{-3}\,\mathrm{m}, \quad x_0 = \sqrt{\frac{\lambda_0 z_0}{2\pi\bar{n}}}, \quad t_0 = \frac{n_g z_0}{c_0},$$

where $\lambda_0 = 973\mathrm{nm}$, $\bar{n} = 3.2262$, $n_g = 3.66$ and c_0 are the central wavelength, the background refractive index, the group velocity index, and the speed of light in vacuum, respectively.

The dynamics of the device is defined by the spatio-temporal evolution of the dimensionless functions

$$E^{\pm}(z,x,t) = \frac{E^{\pm}_{orig}}{\sqrt{10^{21}\,\mathrm{m}^{-3}}}, \quad p^{\pm}(z,x,t) = \frac{p^{\pm}_{orig}}{\sqrt{10^{21}\,\mathrm{m}^{-3}}}, \quad N(z,x,t) = \frac{N_{orig}}{10^{24}\,\mathrm{m}^{-3}},$$

denoting complex counter-propagating slowly varying amplitudes of optical fields, complex dielectric dispersive polarization functions, and a real excess carrier density, respectively. All these functions are governed by the $(2+1)$–dimensional traveling wave model

$$\begin{aligned}
&\frac{\partial E^{\pm}}{\partial t} \pm \frac{\partial E^{\pm}}{\partial z} = -\frac{i}{2}\frac{\partial^2 E^{\pm}}{\partial x^2} - i\beta(N,|E^{\pm}|^2)E^{\pm} - i\kappa^{\mp}E^{\mp},\\
&\frac{\partial p^{\pm}}{\partial t} = i\omega_p p^{\pm} + \gamma_p\big(E^{\pm} - p^{\pm}\big),\\
&\frac{1}{\mu}\frac{\partial N}{\partial t} = \frac{\partial}{\partial x}\Big(D\frac{\partial N}{\partial x}\Big) + J(z,x) - R(N) - \Re e\sum_{\nu=\pm} E^{\nu *}\left[G(N,|E^{\pm}|^2) - \mathcal{D}\right]E^{\nu},
\end{aligned} \tag{2.1}$$

where $i = \sqrt{-1}$ is an imaginary unit and * denotes a complex conjugate. Operators β, $\mathcal{D}$ and functions G, $\tilde{n}$, R denote the propagation factor, Lorentzian approximation of the material gain dispersion, the refractive index change, the spontaneous recombination of carriers, and the gain peak value, respectively:

$$\begin{aligned}
&\beta(N,|E^{\pm}|^2) = \Delta\,\chi_3(z,x) - \tilde{n}(N) + 0.5i\left(G(N,|E^{\pm}|^2) - \alpha - \mathcal{D}\right),\\
&\mathcal{D}E^{\pm} = g_p\big(E^{\pm} - p^{\pm}\big), \quad \tilde{n}(N) = 2\sigma n_{tr}\sqrt{N/n_{tr}}, \quad R(N) = AN + BN^2 + CN^3,\\
&G(N,|E^{\pm}|^2) = \frac{g' n_{tr}}{1 + \varepsilon\left(|E^{+}|^2 + |E^{-}|^2\right)}\log\Big(\frac{\max(N,n_*)}{n_{tr}}\Big), \quad 0 < \frac{n_*}{n_{tr}} \ll 1.
\end{aligned}$$

The parameters entering Eqs. (2.1) and used in the notations above are allowed to be spatially non-homogeneous and discontinuous depending on the laser geometry. Actually, we assume that the spatial domain $Q_{z,x}$ is composed of m

non-intersecting parts S_j ($\bar{Q}_{z,x} = \cup_{j=1}^{m} \bar{S}_j$, $\bar{\Omega}$ is the closure of the domain Ω), and within each S_j any parameter P is given by some constant P_j:

$$P = P(z,x) = \sum_{j=1}^{m} P_j \chi_j(z,x), \quad \text{where} \quad \chi_j(z,x) = \begin{cases} 1, & \text{if } (z,x) \in S_j \\ 0, & \text{elswhere} \end{cases}.$$

More details about meaning and typical values of these parameters can be found in Table 1 and Refs. [3, 8].

We complete the description of the mathematical model by specifying reflecting boundary conditions of the fields $E^{\pm}$ at the laser facets $z = 0$ and $z = L$ defined on $\bar{Q}_{x,t} = \mathbb{R} \times [0,T]$ as

$$E^+(0,x,t) = r_0(x)\, E^-(0,x,t) + a(x,t), \quad E^-(L,x,t) = r_L(x)\, E^+(L,x,t). \tag{2.2}$$

Here, $a(x,t)$ is a complex function representing optically injected optical field, and $r_{0,L}$ are complex reflectivity factors, $|r_{0,L}| \leq 1$ (for optical amplifiers $|r_{0,L}| \to 0$).

The initial conditions (if properly stated) are not very important, since after some transients the simulated trajectories approach one of the existing stable attractors.

Table 1. Typical parameter values.

Symbol	Description	Value
l_1	length of S_1 (MO) & S_3 (trench)	2
l_2	length of S_2 (PA)	2
w_1	width of S_1 & inner edge of S_2	0.4
w_2	width of S_2 at front facet	30
w_3	width of S_3	4.4
$\kappa^{\pm}$	field coupling coefficient	0 or $0.25\,\chi_1$
g'	differential gain	1.8
σ	differential index	1
α	internal absorption	0.15
Δ	index step detuning in the trench (S_3)	-32
n_{tr}	transparency carrier density	1.3
n_*	gain clamping carrier density	0.1
ϵ	nonlinear gain compression	0
g_p	Lorentzian gain amplitude	13
$2\gamma_p$	Lorentzian width at half maximum	$600\,\pi$
ω_p	gain peak detuning	$12\,\pi$
μ	photon/carrier life time relation	10^{-3}
D	carrier diffusion coefficient	0.5
A	spontaneous recombination parameter	3.6
B	spontaneous recombination parameter	2.2
C	spontaneous recombination parameter	0.04
J	injection current density	$400\,\chi_1 + 70\,\chi_2$
r_0	(complex) rear facet field reflectivity	-0.01 or -0.04
r_L	(complex) front facet field reflectivity	0.01 or 0.04

3 Auxiliary Problem

Let us consider propagation or generation of stationary (continuous wave) optical fields in optical amplifiers or lasers with vanishing field coupling factor $\kappa^{\pm}$. In this stationary case the propagation factor β and the optical field intensities $|E^{\pm}|^2$ are fixed in time and depend only on spatial coordinates (z, x). Assume that $E^{+}(0, x, t_0) = u_0(x)$ is given and $\beta(z, x, t) = \mathcal{B}(z, x)$ is fixed and known. Then the linear $1 + 1$ dimensional Schrödinger problem

$$\frac{\partial u}{\partial z} = -\frac{i}{2}\frac{\partial^2 u}{\partial x^2} - i\mathcal{B}(z, x)u, \quad (z, x) \in Q_{z,x}; \quad u(0, x) = u_0(x), \quad x \in \mathbb{R} \tag{3.1}$$

determines the optical field $E^{+}(z, x, t_0 + z) = u(z, x)$ propagating along the characteristic direction $z = t - t_0$. We shall use this auxiliary problem for estimation of the numerical errors induced by the discrete approximations of the diffraction operator on discrete grids with quite large space steps and by artificially induced boundary conditions.

In the numerical experiments below we consider several analytic expressions of $\mathcal{B}(z, x)$ which approximate the static distributions of propagation factor β obtained after integration of the TW model (2.1), (2.2). The real part of $\mathcal{B}$ representing the refractive index at different parts of considered device is mainly determined by the static factor Δ giving the major contribution to $\Re e\beta$ used in Eq. (2.1):

$$\Re e\, \mathcal{B}(z, x) = \begin{cases} \Delta\Big(1 - e^{-\left(\frac{s_i(x)}{\sigma_i}\right)^2}\Big), & \text{if } \ z \in [0, l_1] \ \& \ |x| \in \Big[\frac{w_1}{2}, \frac{w_1}{2} + w_3\Big] \\ 0, & \text{elsewhere,} \end{cases} \tag{3.2}$$

where $s_i(x) = \min\{w_3 - (|x| - w_1/2), |x| - w_1/2\}$, $0 \le \sigma_i \ll 1$.

In the sequel we assume that the index step transition factor $\sigma_i = 0.01$. This implies a 95% growth or fall of $\Re e\mathcal{B}$ during 0.03-long lateral interval. As it will be shown later, such a potential at $z < l_1$ yields an (index) guiding of the optical beam.

The imaginary part of $\mathcal{B}$ determines amplification and losses of the propagating beam. It depends mainly on the carrier distribution $N(z, x)$, which is large at the pumped regions of the laser, can be depleted by large field intensities $|E^{\pm}(z, x)|^2$, and diffusively decays into the unpumped regions. We use the following approximation:

$$\Im m\, \mathcal{B}(z, x) = \begin{cases} 3 - \dfrac{15 s_g^2(z, x)}{1 + s_g^2(z, x)}, & \text{if } \ |x| > \dfrac{w_2 - w_1}{4l_2}\,(|z - l_1| + z - l_1) \\ 3, & \text{elsewhere,} \end{cases} \tag{3.3}$$

where $s_g(z, x) = \min\left\{X_0, |x| - \dfrac{w_2 - w_1}{4l_2}\,(|z - l_1| + z - l_1)\right\}$, $X_0 = 2$. We shall show in the sequel how such a gain profile allows us to realize the (gain) guiding of optical beam even when the potential well is absent (i.e., the case $\Re e\mathcal{B} = 0$).

4 Finite Difference Scheme for the Auxiliary Problem

To solve the auxiliary problem (3.1) we use a uniform grid for the longitudinal interval $z \in [0, L]$ and a non-uniform grid for the lateral domain $x \in \mathbb{R}$:

$$\omega_z = \{z_n : \quad z_n = nh_z, \quad n = 0, \ldots, M, \quad h_z = L/M\},$$
$$\omega_x = \{x_j : \quad x_j = -x_{-j}, \quad h_{x,j-1/2} = x_j - x_{j-1}, \quad j \in \mathbb{Z}\},$$
$$\omega_{zx} = \{(z_n, x_j) : \quad z_n \in \omega_z, \quad x_j \in \omega_x\}.$$

To integrate numerically Eq. (3.1) we use the standard two-layer Crank-Nicolson finite difference scheme

$$\frac{U_j^n - U_j^{n-1}}{h_z} = -i\left[\frac{1}{2}\partial_x\partial_{\bar{x}} + \mathcal{B}(z_{n-1/2}, x_j)\right]\frac{U_j^n + U_j^{n-1}}{2}, \qquad U_j^0 = u_0(x_j), \tag{4.1}$$

where

$$1 \le n \le M, \quad j \in \mathbb{Z}, \tag{4.2}$$

and the grid function U defined on ω_{zx} approximates the solution $u(z,t)$ of Eq. (3.1): $U_j^n \approx u(z_n, x_j)$. The finite difference operators $\partial_{\bar{x}}$ and ∂_x used in (4.1) are given by

$$V_{j-1/2} := \partial_{\bar{x}} U_j^n = \frac{U_j^n - U_{j-1}^n}{h_{x,j-1/2}}, \quad \partial_x V_{j-1/2} = \frac{V_{j+1/2} - V_{j-1/2}}{0.5(h_{x,j-0.5} + h_{x,j+0.5})}.$$

Since the lateral mesh ω_x is infinite, the problem (4.1), (4.2), in general, can not be solved directly. Thus, we truncate our spatial domain $Q_{z,x}$, so that a new domain $\bar{Q}_{z,x}^T = [0, L] \times [-X, X]$ contains all most important (injected) sections of the considered device. The corresponding truncated mesh is given by

$$\omega_{zx}^T = \{(z_n, x_j) : \quad z_n \in \omega_z, \quad x_j \in \omega_x^T\}, \quad \text{where}$$
$$\omega_x^T = \{x_j : \quad x_j = -x_{-j}, \quad h_{x,j-1/2} = x_j - x_{j-1}, \quad j = -J, \ldots, J, \quad x_J = X\}.$$

The numerical scheme (4.1) is considered now for

$$1 \le n \le M, \qquad -J < j < J. \tag{4.3}$$

Boundary conditions. To close the scheme (4.1), (4.3) we need to define the grid function U_j^n on the lateral boundaries of the mesh ω_{zx}^T, where $j = -J$ or $j = J$. In our paper we investigate the performance of three different strategies.

First, assuming the uniform grid and constant potential in the outer region ($h_{x,j\pm0.5} = h_x$ and $\mathcal{B}(x_j, z) = \bar{\mathcal{B}} = \text{const}$ for $|j| \ge J - 1$) and the compact support $\operatorname{supp} u_0(x) \subset (-X, X)$ of the initial function we can use the *exact* discrete transparent boundary conditions (TBC) [1]:

$$U_{\pm(J-1)}^n = \sum_{k=1}^{n} U_{\pm J}^k l^{n-k} - U_{\pm(J-1)}^{n-1}, \tag{4.4}$$

with

$$l^k = (1+iR+\sigma)\,\delta_k^0 + (1-iR+\sigma)\,\delta_k^1 + \xi e^{ik\varphi}\frac{P_k(\mu)-P_{k-2}(\mu)}{2k-1},$$
$$\varphi = \arctan\frac{2R(\sigma+1)}{R^2-2\sigma-\sigma^2},\quad \mu = \frac{R^2+2\sigma+\sigma^2}{\sqrt{(R^2+\sigma^2)\,(R^2+(\sigma+2)^2)}},$$
$$\sigma = -h_x^2\bar{\mathcal{B}},\quad R = \frac{2h_x^2}{h_z},\quad \xi = -i\left[(R^2+\sigma^2)\left(R^2+(\sigma+2)^2\right)\right]^{1/4}e^{-i\varphi/2}.$$

Here δ_k^r is the Kronecker symbol and P_k are the Legendre polynomials ($P_{-2}=P_{-1}\equiv 0$). This formula is a discrete analog of the nonlocal TBC

$$\pm\frac{1}{\sqrt{2}}\frac{\partial}{\partial x}u(z,\pm X) = -\frac{e^{i\pi/4}}{\sqrt{\pi}}e^{-i\bar{\mathcal{B}}z}\frac{d}{dz}\int_0^z\frac{u(s,\pm X)}{\sqrt{z-s}}e^{i\bar{\mathcal{B}}s}ds,$$

valid for the auxiliary problem (3.1). We note, however, that a practical implementation of the exact conditions (4.4) is computationally very expensive, since they require a storage of numerical solutions U_j^n on boundary points $j=-J,J$ for all previous time levels. The kernel l^k in the discrete nonlocal operator decreases quite slowly, thus the truncated TBC (TTBC)

$$U_{\pm(J-1)}^n = \sum_{k=\max(n-q,1)}^{n} U_{\pm J}^k l^{n-k} - U_{\pm(J-1)}^{n-1}, \tag{4.5}$$

obtained by using a small threshold q for memory length in time are not accurate and produce oscillating parasitic reflected waves (see, [6]).

Next, we apply computationally efficient boundary conditions

$$\pm\frac{1}{\sqrt{2}}\frac{U_{\pm J}^{n+1/2}-U_{\pm J\mp 1}^{n+1/2}}{h_x} + \frac{h_x}{\sqrt{2}}\Big(i\frac{U_{\pm J}^{n+1}-U_{\pm J}^n}{h_z} - \bar{\mathcal{B}}U_{\pm J}^{n+1/2}\Big)$$
$$= -i\big(bU_{\pm J}^{n+1/2} + \sum_{k=1}^{m} a_k\big(U_{\pm J}^{n+1/2} - d_k\Phi_k^{\pm,n+1/2}\big)\big),$$
$$\frac{\Phi_k^{\pm,n+1}-\Phi_k^{\pm,n}}{h_z} + i(\bar{\mathcal{B}}+d_k)\Phi_k^{\pm,n+1/2} = iU_{\pm J}^{n+1/2},\quad \Phi_k^{\pm,0}=0,\ \ k=1,\dots,m, \tag{4.6}$$

derived from a standard Crank–Nicolson type discretization of the approximate transparent boundary conditions (ATBC) [14]

$$\pm\frac{1}{\sqrt{2}}\frac{\partial}{\partial x}u(z,\pm X) = -ibu(z,\pm X) - i\sum_{k=1}^{m}a_k\big(u(z,\pm X) - d_k\varphi_k^{\pm}(z)\big),$$
$$\frac{d}{dz}\varphi_k^{\pm}(z) = i\left(u(z,\pm X) - \left(d_k+\bar{\mathcal{B}}\right)\varphi_k^{\pm}(z)\right),\qquad \varphi_k^{\pm}(0)=0,\quad k=1,\dots,m.$$

Here we use the notation $V_j^{n+1/2} = 0.5(V_j^{n+1}+V_j^n)$.

The values of the parameters b, a_k and d_k are obtained by minimizing some specially constructed reflection function. In this paper we assume that

$m = 3$ and use the coefficients $b = 0.7269284$, $a_1 = 2.142767$, $a_2 = 5.742223$, $a_3 = 46.58032$, $d_1 = 6.906263$, $d_2 = 65.82243$, $d_3 = 1124.376$, as it is suggested in [14].

Finally, we use simple Dirichlet boundary conditions (DBC)

$$U^n_{-J} = 0, \quad U^n_J = 0. \tag{4.7}$$

This simple condition is frequently used in the case of the significant damping of the optical beam at the lateral borders of the truncated domain by the (negative) function $\Im m\mathcal{B}(z, x)$.

5 Finite Difference Scheme for the TW Model

The finite difference schemes of the Crank-Nicolson type for the full TW model were described in our previous publication [7]. We remind here only some most relevant aspects of these schemes and propose some modifications in approximation of the polarization functions $p^{\pm}$.

To construct the finite difference schemes for the TW model (2.1), (2.2) we introduce additionally the uniform temporal mesh ω_t and the staggered temporal and longitudinal meshes $\omega_t^\bullet$ and $\omega_z^\bullet$:

$$\begin{aligned}
\omega_t &= \{t_n : \ t_n = nh_z, \quad n = 0, \dots, K = T/h_z\},\\
\omega_t^\bullet &= \{t_{n-0.5} : \ t_{n-0.5} = (n-0.5)h_z, \quad n = 1, \dots, K\},\\
\omega_z^\bullet &= \{z_{k-0.5} : \ z_{k-0.5} = (k-0.5)h_z, \quad k = 1, \dots, M\}.
\end{aligned}$$

The fields $E^{\pm}$ and polarization functions $p^{\pm}$ are approximated on the truncated mesh ω_E, and the carrier density N is approximated on the truncated mesh ω_N, where:

$$\begin{aligned}
\omega_E &= \{(z_k, x_j, t_n) : \ (z_k, x_j) \in \omega^T_{z,x}, \ \ t_n \in \omega_t\},\\
\omega_N &= \{(z_{k-0.5}, x_j, t_{n-0.5}) : \ z_{k-0.5} \in \omega_z^\bullet, \ \ t_{n-0.5} \in \omega_t^\bullet, \ \ x_j \in \omega_x^T\}.
\end{aligned}$$

We note, that equal temporal and longitudinal steps $h_t = h_z$ are used, what allows us to simulate exactly the propagation of the grid field functions $E_h^{\pm}$ along characteristic lines $z = t - t_0$ and $L - z = t - t_0$.

In contrast to [7], we treat the lateral boundaries of the field functions in a different manner. We assume, that the outer lateral regions of the laser device are rather simple, i.e., they are not pumped, there is no direct counter-propagating field coupling, and the impact from the polarization equations can be neglected there:

$$J(x, z) = 0, \quad \kappa^{\pm}(x, z) = 0, \quad g_p(x, z) = 0 \quad \text{for all} \quad |x| \geq X.$$

We assume, that a small optical field intensity within this outer region $|x| \geq X$ is not sufficient for more or less significant pumping of the otherwise well damped carriers. Thus, we set Dirichlet boundary conditions

$$N^{n-0.5}_{h,k-0.5,-J} = 0, \ \ N^{n-0.5}_{h,k-0.5,J} = 0, \quad k = 1, \dots, M, \ \ n = 1, \dots, K \tag{5.1}$$

and, consequently, get that

$$\beta(N,|E^{\pm}|^2)=\beta(x,z,t)=\mathcal{B}(z),\quad \text{for all}\quad |x|\geq X.$$

That is, in the outer lateral region the optical field equations in Eq. (2.1) are decoupled from the polarization and carrier equations and, in general, they are equivalent to our auxiliary problem (3.1). Thus, when calculating the grid optical field functions $E_h^{\pm}$ we can use the boundary conditions considered above for the auxiliary problem.

Next we give a brief description of the finite difference scheme used to solve the full TW model (2.1)–(2.2). For more details see [7]. Let us assume that we know the grid functions $E_h^{\pm}$ and $p_h^{\pm}$ at the time layer t_n and the grid function N_h at $t_{n-0.5}$.

Discrete carrier equation. In the first step we construct a standard Crank-Nicolson type scheme for carrier densities N approximating the corresponding TW model equation at points $(z_{k-0.5},x_j,t_n)$. It can be written in the form

$$\begin{aligned}&\frac{N^{n+0.5}_{h,k-0.5,j}-N^{n-0.5}_{h,k-0.5,j}}{h_z}\\&\quad=F_N\Big(\frac{N^{n+0.5}_{h,k-0.5,j}+N^{n-0.5}_{h,k-0.5,j}}{2},E^{\pm,n}_{h,k,j},E^{\pm,n}_{h,k-1,j},p^{\pm,n}_{h,k,j},p^{\pm,n}_{h,k-1,j}\Big).\end{aligned}\tag{5.2}$$

After setting the Dirichlet boundary conditions at x_{-J} and x_J, we can resolve this scheme with respect to N_h at $t_{n+0.5}$ by means of the standard factorization method using predictor-corrector procedure to treat nonlinearities implied by the functions R and G.

Discrete field and polarization equations. In the next step we construct the Crank–Nicolson type schemes approximating field equations at $(z_{k-0.5},x_j,$ $t_{n+0.5})$, while the field transport along characteristics is approximated as

$$\Big(\frac{\partial}{\partial t}+\frac{\partial}{\partial z}\Big)E^{+}\approx\frac{E^{+,n+1}_{h,k,j}-E^{+,n}_{h,k-1,j}}{h_z},\quad \Big(\frac{\partial}{\partial t}-\frac{\partial}{\partial z}\Big)E^{-}\approx\frac{E^{-,n+1}_{h,k-1,j}-E^{-,n}_{h,k,j}}{h_z}.$$

The resulting schemes for the optical fields can be written in the form

$$\frac{E^{+,n+1}_{h,k,j}-E^{+,n}_{h,k-1,j}}{h_z}=F^{+}_{E}\Big(\frac{E^{+,n+1}_{h,k,j}+E^{+,n}_{h,k-1,j}}{2},\frac{p^{+,n+1}_{h,k,j}+p^{+,n}_{h,k-1,j}}{2},N^{n+0.5}_{h,k-0.5,j}\Big),\tag{5.3}$$

$$\frac{E^{-,n+1}_{h,k-1,j}-E^{-,n}_{h,k,j}}{h_z}=F^{-}_{E}\Big(\frac{E^{-,n+1}_{h,k-1,j}+E^{-,n}_{h,k,j}}{2},\frac{p^{-,n+1}_{h,k-1,j}+p^{-,n}_{h,k,j}}{2},N^{n+0.5}_{h,k-0.5,j}\Big).\tag{5.4}$$

Differential equations for the polarization functions at $(z_k,x_j,t_{n+0.5})$ are approximated by the following exponentially fitted discrete scheme

$$p^{\pm,n+1}_{h,k,j}=F^{\pm}_{p}\left(p^{\pm,n}_{h,k,j},E^{\pm,n+1}_{h,k,j},E^{\pm,n}_{h,k,j}\right),\tag{5.5}$$

$$F^{\pm}_{p}=e^{-\tilde{\gamma}_p h_z}\big(p^{\pm,n}_{h,k,j}-\frac{\gamma_p}{\tilde{\gamma}_p}E^{\pm,n}_{h,k,j}\big)+\frac{\gamma_p}{\tilde{\gamma}_p}E^{\pm,n+1}_{h,k,j}-\frac{\gamma_p}{\tilde{\gamma}_p^2}\frac{E^{\pm,n+1}_{h,k,j}-E^{\pm,n}_{h,k,j}}{h_z}\big(1-e^{-\tilde{\gamma}_p h_z}\big),$$

where $\tilde{\gamma}_p = \gamma_p - i\omega_p$. It follows from the given formula, that the asymptotic equality $p^{\pm,n+1}_{h,k,j} \approx \frac{\gamma_p}{\tilde{\gamma}_p} E^{\pm,n+1}_{h,k,j}$ is valid for $|\tilde{\gamma}_p| \gg 1$. It is easy to prove that the accuracy of this approximation is $O(h_z^2)$.

To resolve the schemes (5.3)-(5.5) we substitute function $p^{\pm,n+1}_{h,i,j}$ from (5.5) into (5.3)–(5.4) and solve the obtained system of linear equations by using the block version of the factorization algorithms, where the size of the blocks is 2×2. Then the polarization vectors are computed from the explicit relations (5.5). All nonlinearities in coefficients are linearized by using the predictor-corrector procedure.

6 Numerical Study of the Auxiliary Problem

Within this section we analyze the precision of the numerical schemes (4.1),(4.3) with boundary conditions (4.5), (4.6), or (4.7) for the auxiliary problem (3.1). The global computational error $r^n_{f,j} = U^n_j - u(z_n, x_j)$ estimated on the grid ω^T_{zx} is determined by the approximation accuracy of the discrete scheme (4.1) – (4.2), and by the errors induced by discrete boundary conditions:

$$|r^n_{f,j}| \le |r^n_{h,j}| + |r^n_{BC,j}|, \quad \text{where} \quad r^n_{h,j} = U^n_{ex,j} - u(z_n, x_j),\ r^n_{BC,j} = U^n_j - U^n_{ex,j}. \tag{6.1}$$

Here by $U^n_{ex,j}$ and U^n_j we denote solutions of (4.1), (4.3) with exact (4.4) or imperfect (4.5)–(4.7) boundary conditions, respectively.

A case of vanishing potential $\mathcal{B}$. To distinguish the contribution of these two error sources we compute and compare discrete approximations of the function

$$u(z,x) = \left[\frac{2w_0}{2w_0 - iz}\,\exp\left(-ik(2x-kz) - \frac{(x-kz)^2}{(2w_0 - iz)}\right)\right]^{1/2},$$

which is the solution of Eq. (3.1) with $\mathcal{B}(z,x) \equiv 0$ and the initial condition

$$u_0(x) = u(0,x) = e^{-x^2/(4w_0)} e^{-ikx}. \tag{6.2}$$

Here, $\sqrt{w_0}$ scales the beam width, and $k \neq 0$ is responsible for the beam propagation towards the lateral bound of the domain. If not indicated explicitly, we assume that $w_0 = 0.1$, $k = 2$, perform our simulations in the domain defined by $X = 2.56$ and $L = 2$ and use a uniform grid. We represent only those values of the numerical solutions U^n_j or $U^n_{ex,j}$ which are defined on the grid points (z_n, x_j) belonging to a smaller *observation* domain $[0, L] \times [-\tilde{X}, \tilde{X}]$, $\tilde{X} = 2$. So that the relative maximum norms of the solution errors discussed bellow are defined as

$$\varepsilon_s(z_n) = \frac{\max_{|x_j|\le\tilde{X}}(|r^n_{s,j}|)}{\max(10^{-2}, \max_{|x_j|\le\tilde{X}}(|V^n_j|))},\ \ \|\varepsilon_s\|_C = \max_{z_n\in[0,L]}(\varepsilon_s(z_n)),\ \ s \in \{f, h, BC\},$$

where $V^n_{BC,j} = U^n_{ex,j}$ and $V^n_{s,j} = u(z_n, x_j)$ for $s \in \{f, h\}$.

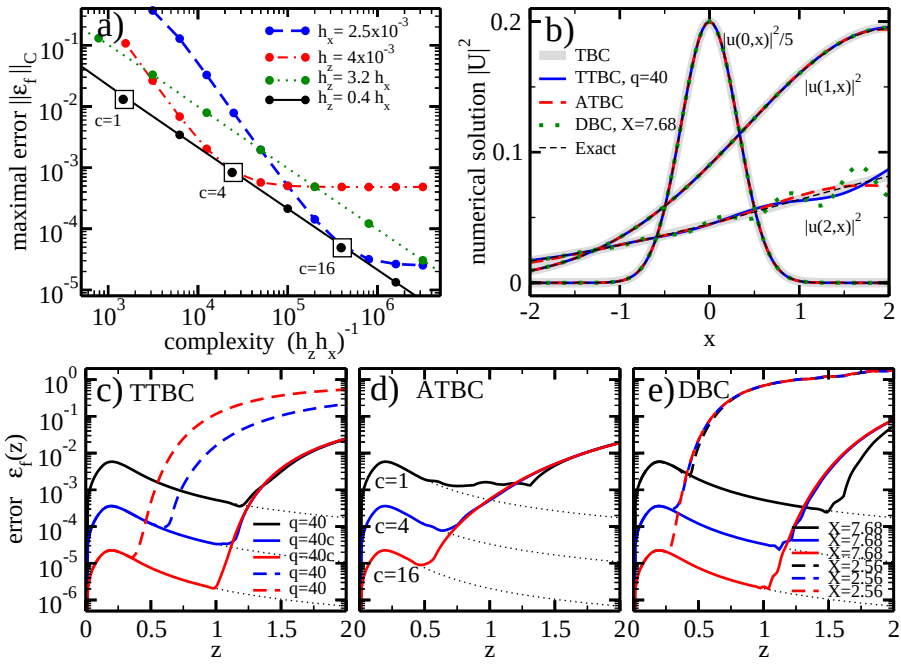

Figure 2. Representation of numerical solutions to Eqs. (3.1), (6.2) with $\mathcal{B} \equiv 0$ using the scheme (4.1), (4.3) with different BC (4.4)–(4.7). (a): Dependence of $\|\varepsilon_h\|_C$ on h_z and h_x for the scheme with the exact TBC (4.4). Numerical experiments (bullets) were done keeping fixed relations between h_z and h_x (see curve labels). Squares indicate grid steps used in panels (b-e). (b): $|U_j^n|^2$ for different BC, $|U_{ex,j}^n|^2$ and $|u(z_n, x)|^2$ at $z_n \in \{0, 1, 2\}$. Grid steps: (6.3) with $c = 1$. (c,d,e): Evolution of $\varepsilon_f(z_n)$ for the solution of the schemes with TTBC (4.5), ATBC (4.6) and DBC (4.7), respectively. Dotted curves: reference errors $\|r_h(z_n)\|_C$ obtained using the exact TBC (4.4). Upper (black), middle (blue) and lower (red) curves correspond to the grid steps (6.3) with $c = 1$, $c = 4$ and $c = 16$, respectively.

First, we consider the scheme (4.1), (4.3) with the exact TBC (4.4). The solution error $r_{f,j}^n = r_{h,j}^n = \mathcal{O}(h_x^2 + h_z^2)$ in this case is determined only by the Crank-Nicolson scheme (4.1), but not by some boundary condition imperfections. [1] The scheme (4.1) is unconditionally stable. However, to optimize the performance of computations, i.e., to minimize the number of arithmetic operations $\sim (h_z h_x)^{-1}$ needed to achieve the required precision $\sim (h_z^2 + \gamma^2 h_x^2)$, we keep the ratio $h_z \approx \gamma h_x$ with $\gamma \in \mathbb{R}_+$ depending on the initial conditions. This is illustrated by Fig. 2(a) representing the dependence of the maximal relative error $\|\varepsilon_f\|_C$ on the simulation complexity $(h_z h_x)^{-1}$. The smallest error of the scheme at some fixed complexity could be achieved when selecting grid steps according to $h_z = 0.4 h_x$: see black solid line in Fig. 2(a). The squares on this line indicate the grid steps

$$h_x = 0.04/c, \qquad h_z = 0.4 h_x = 0.016/c, \tag{6.3}$$

[1] Actually, by setting X and $U_{\pm J}^0 = 0$ we introduce initial boundary errors $r_{BC,\pm J}^0 \sim 10^{-7}$, which remain negligible for the full error $r_{f,j}^n$ for h_x and h_z used in our simulations.

with $c \in \{1, 4, 16\}$, which we use in all our simulations discussed below in this section.

Several numerical solutions U_j^n for different BC at $z_n = 1$ and $z_n = 2$ are shown in Fig. 2(a). Here we use rather large grid steps (6.3) with $c = 1$, a larger computational domain defined by $X = 7.68$ for DBC (4.7), and the truncation bound $q = 40$ for TTBC (4.5). All these numerical solutions are in a good agreement with the exact solution $u(z_n, x)$ and the exact numerical solution $U_{ex,j}^n$ at $z_n = 1$. At $z_n = 2$, however, the errors introduced by non-exact BC start to be visible.

The impact of the BC imperfections can be better understood when analyzing panels (c-e) of Fig. 2. For small z all numerical solutions corresponding to the same grid steps are coinciding. That is, up to some critical z^* we do not feel the impact of the BC, the solution error $r_{f,j}^n \approx r_{h,j}^n$ depends only on the grid steps (6.3) and is scaled by the factor c^{-2}. For larger z the total error $r_{f,j}^n$ is dominated by the BC imperfections $r_{BC,j}^n$ and is nearly independent on the grid steps: see triples of curves corresponding to $c = 1$, 4 and 16 coming together for larger z in panels (d) and (e). In the case of TTBC (panel c) the decrease of h_z requires also a corresponding increase of the factor q. Otherwise, at larger z we get a significant growth of the BC implied errors $r_{BC,j}^n$.

We can reduce the error $r_{BC,j}^n$ by increasing X, by increasing q for TTBC (4.5), or by increasing m with a corresponding change of coefficients b, a_k and d_k for ATBC (4.6). All these possibilities, however, are slowing down the computations. On the other hand, if the full error $r_{f,j}^n$ of the numerical solutions shown in Fig. 2(b) is sufficiently small, we should not waist CPU time for computations with too small grid steps. It is enough to select the steps at which the scheme (4.1) implied error $\varepsilon_h(z)$ is similar to the error $\varepsilon_{BC}(z)$ induced by imperfect BC. This situation is represented by the black solid curves ($c = 1$) in Fig. 2(c-e).

Let us compare these three approaches. In the case of DBC (panel e) our boundary conditions are very simple, but we waist CPU time by resolving our problem in a 3 times larger domain. A choice of smaller X leads to a drastic increase of errors (dashed lines in panel e). In the case of TTBC (panel c) we keep the boundary values of the solution at $q = 40$ previous z-steps and compute a convolution sum at each new iteration. A smaller q leads to an increase of errors. Finally, in the case of ATBC (panel d) we keep the values of only $m = 3$ functions Φ_k and modify them according to (4.6) after each iteration.

An index-guiding case. Let us consider again the problem (3.1),(6.2) assuming $\Im m\mathcal{B} \equiv 0$ and $\Re e\mathcal{B}$ defined by Eq. (3.2). In contrast to the zero-$\mathcal{B}$ case such a potential well (a step in $\Re e\mathcal{B}$) allows to confine and to guide the optical beam along the longitudinal z-axis (compare the numerical solutions in Figs. 2b and 3a). As a consequence, only relatively small beam tails are radiated out from the domain of observation. For this reason, we can set $X = 0.96$ and $\tilde{X} = 0.8$ assuming a much smaller computation and observation domains. To suppress the wings of the initial function (6.2) at $x = \pm X$ we take $w_0 = 0.025$. This allows us to avoid BC implied imperfections when using exact TBC (4.4)

and, therefore, to distinguish the contributions of the solution errors $r^n_{h,j}$ and $r^n_{BC,j}$.

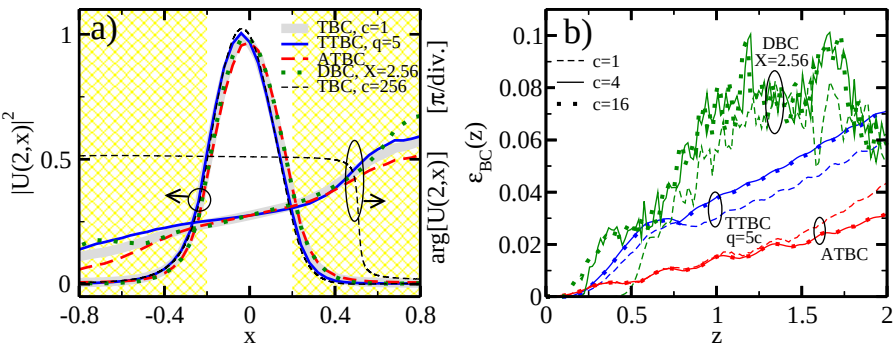

Figure 3. Representation of the numerical solutions to Eqs. (3.1), (3.2), (6.2) with $\Im m\mathcal{B} \equiv 0$. (a): Intensity and phase of $U^M_{ex,j}$ and U^M_j for different BC at $z_M = L = 2$. Grid steps: (6.3) with $c = 1$ (except of the dashed curves computed with $c = 256$). Yellow shading: location of the trenches. (b): Evolution of $\varepsilon_{BC}(z_n)$ for the solution of the schemes with TTBC (4.5), ATBC (4.6) and DBC (4.7), and the grid steps (6.3) with $c \in \{1, 4, 16\}$.

First, we have checked the performance of the scheme (4.1), (4.3), (4.4) using grid steps (6.3) with different factors c. For estimation of the error $r^n_{h,j}$ we substitute the unknown exact solution $u(z_n, x_j)$ in Eq. (6.1) by the numerical solution $U^n_{ex,j}$ computed using factor $c = 512$. We have found, that for $c = 1$ the maximal relative error $\|\varepsilon_h\|_C$ can be of order 1. Only by taking $c \geq 4$ we could achieve the required $\sim 10^{-2}$ precision.

The main source of the error is a lack of precision in computation of the beam phase $\phi(z, x) = \arg(u(z, x))$ governed by the equation

$$\frac{\partial\phi}{\partial z} = -\frac{1}{4v}\frac{\partial^2 v}{\partial x^2} + \frac{1}{8v^2}\left(\frac{\partial v}{\partial x}\right)^2 - \frac{1}{2}\left(\frac{\partial\phi}{\partial x}\right)^2 - \Re e\mathcal{B}$$

derived from Eq. (3.1), while the beam intensity $v = |u(z, x)|^2$ can be recovered quite well even with $c = 1$: compare corresponding thin dashed ($c = 256$) and thick grey ($c = 1$) curves in Fig. 3(a). Actually, this beam phase error is due to the large gradients or discontinuities, which are implied by the index step detuning Δ defining the potential $\Re e\mathcal{B}(z, x)$ in (3.2). This error can be decreased either by taking finer grid steps, or, alternatively, by assuming a smaller detuning step Δ, a larger waveguide width w_1 or a larger index step transition factor σ_i.

Next, we have performed simulations of (4.1), (4.3) using BC (4.5)–(4.7). We have found, that it is sufficient to take $q = 5c$ for TTBC (4.5) and $X = 2.56$ for DBC (4.7) in order to guarantee a $10^{-2} - 10^{-1}$ bound of $\varepsilon_{BC}(z)$. Like in zero potential case, these errors are independent of the grid steps (6.3) for $c \geq 4$ (see an agreement between dotted and solid curves in Fig. 3b). Thus, the precision of the numerical solutions can be improved following suggestions discussed in vanishing $\mathcal{B}$ case.

Gain-guiding along a narrow waveguide. In this case we consider our problem (3.1), (6.2) with $w_0 = 0.025$ and assuming $\Re e\mathcal{B} \equiv 0$ and $\Im m\mathcal{B}$ defined by Eq. (3.3). Here again we take $L = l_1 = 2$, i.e., consider only a narrow waveguide region were optical beam is amplified ($\Im m\mathcal{B} > 0$), while at the outer part of this region it is absorbed ($\Im m\mathcal{B} < 0$). An interplay between an amplification of the central part of the beam and an absorption of the beam tails implies confinement and guiding of the optical beam along z-axis.

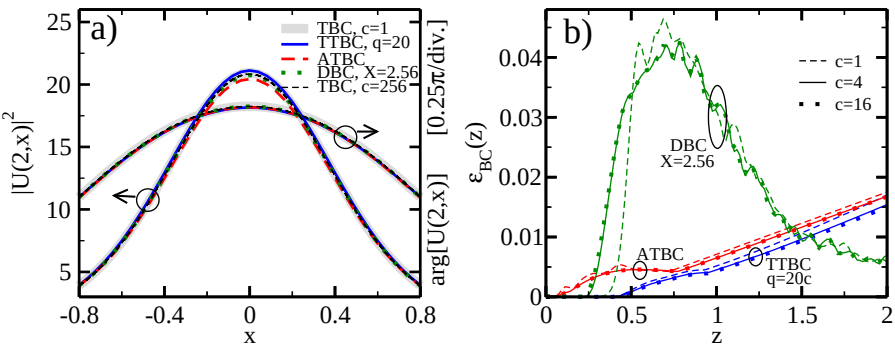

Figure 4. Representation of the numerical solutions to Eqs. (3.1), (3.3), (6.2) with $\Re e\mathcal{B} \equiv 0$. The meaning of both panels is the same as in Fig. 3.

As in the previous case we have estimated the grid induced error $r^n_{h,j}$. Since in this case we had no rapidly changing potential, the relative error norm $\|\varepsilon_h\|_C$ was bounded by factor 0.05 already for the grid steps (6.3) with $c = 1$, and was decaying quadratically with increase of c.

Fig. 4 shows numerically computed functions U^n_j at $z_n = 2$ (panel a) and evolution of $\varepsilon_{BC}(z)$ for different grid step factors c and boundary conditions (4.5)–(4.7). We can conclude from these figures that the effective simulations of our problem can be done with relatively sparse grid steps (6.3) (with, e.g., $c = 1$) and using any of the discussed BC (4.5)–(4.7). The main possible source of errors in this case could be a selection of too small computational domain border X or truncation factor q for TTBC (4.5).

We note also, that during propagation along z-axis both intensity and phase of the beam obtain an axial symmetry (see Fig. 4a). This effect was observed not only for initial conditions (6.2) with different factors k and w_0, but also for initial functions u_0 having a fast π-phase shift in the middle.

Mutual gain- and index-guiding. Let us consider the problem (3.1), (6.2) with $w_0 = 0.025$ and the function $\mathcal{B}$ defined by Eqs. (3.2) and (3.3) for $L = l_1 = 2$. As it could be expected, the major contribution to the numerical solution error is implied by numerical grid and is again due to sharp transitions of $\Im m\mathcal{B}$: compare, e.g., beam phases computed using exact TBC (4.4) and the grid steps (6.3) with $c = 1$ (thick grey curve in Fig. 5a) and $c = 256$ (thin black dashed line in the same figure). At the same time, the errors induced by imperfect BC in this case are relatively low for all considered types of BC (see Fig. 5b). This is due to both an effective beam confinement within the

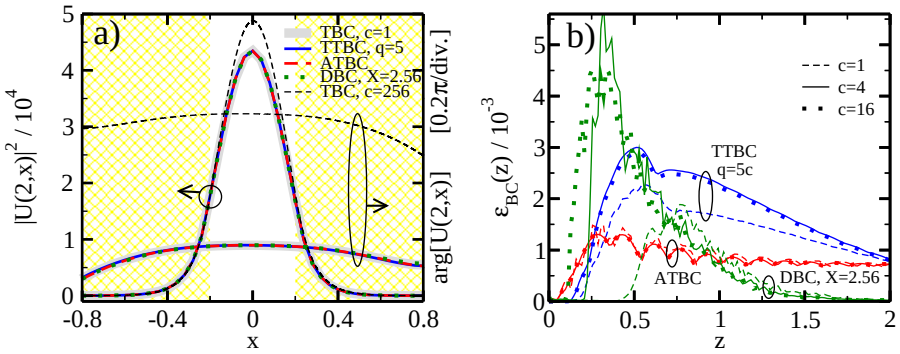

Figure 5. Representation of the numerical solutions to Eqs. (3.1), (3.2), (3.3), (6.2). The meaning of both panels is the same as in Figs. 3 and 4.

narrow waveguide $|x| \le w_1/2$ implied by the index-guiding potential $\Re e\mathcal{B}$ and an absorption of the beam wings for $|x| \to X$ by $\Im m\mathcal{B} < 0$.

We note also, that a mutual beam confinement and its amplification leads to the decay of the beam radiation through the lateral bounds and a significant growth of its amplitude within the waveguide (compare beam intensities in Figs. 4a and 5a).

Beam amplification in tapered amplifier. We consider now the beam propagation in the full domain consisting of a narrow waveguide and a tapered amplifier. For this reason we solve and analyze the problem (3.1), (3.2), (3.3), (6.2) with $w_0 = 0.025$ in the domain defined by $L = l_1 + l_2 = 4$, $X = 18$ and $\tilde{X} = 16 > w_2/2$.

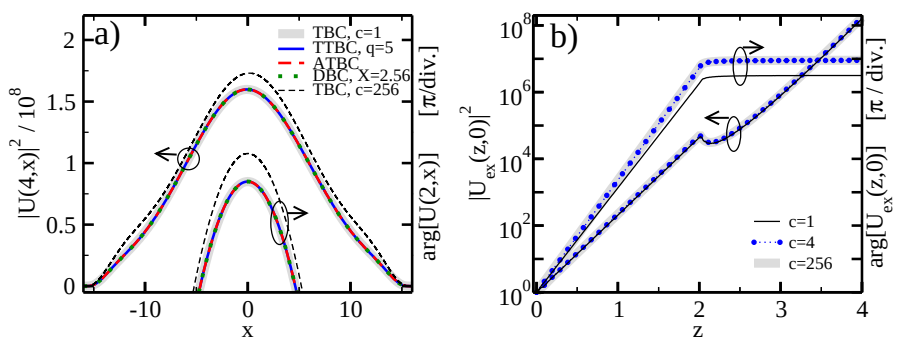

Figure 6. Representation of the numerical solutions to Eqs. (3.1), (3.2), (3.3), (6.2) in the domain defined by $L = 4$, $X = 18$ and $\tilde{X} = 16$. (a): Intensity and phase of $U^M_{ex,j}$ and U^M_j for different BC at $z_M = 4$. Grid steps: (6.3) with $c = 1$ (except of the dashed curves computed with $c = 256$). (b): Intensity and phase evolution of $U^n_{ex,0}$ computed using $c \in \{1, 4, 256\}$.

For the numerical integration of this problem we have used the scheme (4.1), (4.3) supplemented by different BC (4.4)–(4.7). We have found that for all considered BC, namely for DBC with $X \ge 18$, for ATBC with $m = 3$

and for TTBC with $q \geq 5$ the BC induced error $\|\varepsilon_{BC}\|_c$ was kept below 10^{-5} independently on the grid steps (6.3) with $c \geq 1$. That is we have shown that field reflections at the lateral boundary $x = \pm X$ of the domain are effectively absorbed here by $\Im m\mathcal{B} < 0$.

Like in other considered index-guiding cases a full error $r^n_{f,j}$ of the numerical solution is dominated by the numerical grid induced error $r^n_{h,j}$. That is, in order to guarantee $\|\varepsilon_h\|_c \leq 10^{-2}$ we needed to take the grid steps (6.3) with $c \geq 4$. Like in the above mentioned cases, $c = 1$ has also allowed a quite proper reproduction of the beam intensity, while the large error ε_h was mainly induced by the mismatch of the beam phases (compare corresponding thick grey and thin black dashed curves in Fig. 6a).

We note, however, that for $c = 1$ the error growth (growth of the phase mismatch) occurs mainly within the narrow index-guiding region for $z \in [0, l_1]$: see an increasing separation between thick grey and thin black lines in Fig. 6(b) representing evolution of the beam phase along z-axis at $x = 0$. This phase mismatch and, therefore, errors stop growing once the beam leaves the narrow waveguide at $z = 2$.

In conclusion, we have found that a choice of an appropriately fine grid steps for the narrow waveguide possessing sharp transitions of $\Re e\mathcal{B}$ (steps (6.3) with $c \geq 4$ in our case) is a crucial requirement when seeking to get an acceptable precision of the numerical solution. On the other hand, the simulation of the gain guiding, or beam propagation in the tapered amplifier can be done on some more sparse grids. This suggests usefulness of the numerical mesh which is nonuniform in the lateral direction.

7 Parallel Numerical Algorithm for the Full TW Model

The finite difference scheme (5.2)–(5.5) is defined on the structured staggered grid and the complexity of computations at each node of the grid is approximately the same. For such problems the parallelization of the algorithm can be done by using domain decomposition paradigm, as this was done in [7].

We note that the block factorization algorithm used for solution of the block three-diagonal systems of linear equations is fully sequential in its nature. Thus we restrict to 1D block domain decomposition algorithm, decomposing the grid only in z direction. Let us denote by $\omega_z(k)$ the subgrid belonging to the k-th processor $\omega_z(k) = \{z_i : i_{k,L} \leq i \leq i_{k,R}\}$. Here the local sub-domains are not overlapping, i.e. $i_{k,L} = i_{k-1,R} + 1$.

In order to implement the algorithm for the local part of its grid, a processor must exchange some data with its neighbor-processors. The information to be exchanged mainly depends on the stencils of the grid used to approximate differential equations by the discrete scheme. For the finite difference scheme (5.2)–(5.5) two different stencils are used to approximate waves moving in opposite directions. Each processor extends its local subgrid by one ghost point on the left and right sides:

$$\widetilde{\omega}_z(k) = \{z_i : \widetilde{i}_{k,L} \leq i \leq \widetilde{i}_{k,R}\},\ \widetilde{i}_{k,L} = \max(i_{k,L}-1, 0),\ \widetilde{i}_{k,R} = \min(i_{k,R}+1, M).$$

The data exchange algorithm is defined in the following way: after each predictor and corrector step (5.3)–(5.4), the k-th processor

- sends to $(k+1)$ processor vector $E^{+,n+1}_{h,i_{k,R}}$ and receives from it vector $E^{-,n+1}_{h,\widetilde{i}_{k,R}}$,
- sends to $(k-1)$ processor vector $E^{-,n+1}_{h,i_{k,L}}$ and receives from it vector $E^{+,n+1}_{h,\widetilde{i}_{k,L}}$.

We note that vectors $p^{n+1}_{h,i,\cdot}$, $p^{n+1/2}_{h,i-1/2,\cdot}$ are computed locally by each processor and no communications of their values at ghost points are required.

Next we present the main points of the scalability analysis. The complexity of the sequential algorithm for one time step is given by $W = \gamma M(2J+1)$, where γ estimates the CPU time required to implement one basic operation of the algorithm. We assume that communication between neighbor processors is implemented in parallel. Thus the total complexity of the parallel algorithm is equal to

$$T_p = \gamma\big(\lceil (M+1)/p\rceil + 1\big)(2J+1) + 2\big(\alpha + \beta(2J+1)\big).$$

This formula includes costs of extra computations for ghost points, α denotes the message startup time and β is the time required to send one element of data.

The scalability analysis of any parallel algorithm enables us to find the rate at which the size of problem W needs to grow up with respect to the number of processors p in order to maintain fixed the theoretical efficiency $E_p = \frac{W}{pT_p}$ of the parallel algorithm. After simple computations we write the isoefficiency function as a function which relates the number of grid points in z coordinate M to the efficiency of the parallel algorithm E_p and the number of grid points in the x coordinate $2J+1$ (see, [7]):

$$M = \frac{E_p}{1-E_p}\left[\Big(1 + 2\frac{\beta}{\gamma} + 2\frac{\alpha}{\gamma(2J+1)}\Big)p + 1\right].$$

We get two simple conclusions from this formula.

1. In order to maintain a fixed efficiency E_p of the parallel algorithm it is sufficient to increase the number of grid ω_z points linearly with respect to the number of processors p (the size of grid ω^T_x is assumed to be fixed).
2. The increase of J reduces the influence of the message startup time, i.e. a smaller number of M is required to guarantee the prescribed efficiency E_p.

The parallel algorithm was implemented by using the mathematical objects library ParSol [5, 7]. This tool is written using MPI library and it implements some important linear algebra objects in C++. Due to object oriented structure with both sequential and parallel classes of the same objects, ParSol allows to parallelize semi-automatically data parallel algorithms on distributed and shared memory computers.

In order to investigate the efficiency of the parallel discrete algorithm (5.2)–(5.5), we have solved problem (2.1)–(2.2) for different sizes of grids used to approximate the differential problem. The dynamics of laser waves was simulated till 0.2 ns. All parameters of the mathematical model were taken from Table 1, in particular the length of the device $L = 4$ mm. The discretization was done on three discrete grids with $(M + 1) \times (2J + 1)$ elements, where $(M = 400, 2J = 500)$, $(M = 800, 2J = 500)$ and $(M = 800, 2J = 1000)$ respectively. The computations were done on the Vilkas cluster at Vilnius Gediminas technical university. It consists of Intel Quad i7-860 processors (2.80 GHz) interconnected via Gigabit Smart Switch (http://vilkas.vgtu.lt). Obtained performance results are presented in Table 2. Here for each number of processors p the coefficients of the algorithmic speed up $S_p = T_1/T_p$ and efficiency $E_p = S_p/p$ are presented. T_p denotes the CPU time required to solve the problem using p processors. We have investigated the dependence of the performance results on the number of cores used per one node, where $p = n_p \times n_c$, here n_p denotes the number of nodes and n_c denotes the number of cores per node.

Table 2. Results of computational experiments on Vilkas cluster.

	$S_p(1)$	$E_p(1)$	$S_p(2)$	$E_p(2)$	$S_p(3)$	$E_p(3)$
2×1	1.908	0.954	1.902	0.951	1.816	0.908
1×2	1.852	0.926	1.778	0.889	1.783	0.891
4×1	3.778	0.944	3.741	0.935	3.667	0.917
2×2	3.586	0.896	3.613	0.903	3.561	0.890
1×4	3.219	0.804	3.201	0.800	3.133	0.783
8×1	7.478	0.935	7.434	0.929	7.253	0.907
4×2	7.006	0.876	7.096	0.887	6.717	0.840
2×4	6.379	0.797	6.313	0.789	6.180	0.773
8×2	13.28	0.830	13.64	0.853	13.22	0.826
4×4	12.71	0.794	12.54	0.784	12.20	0.762
8×4	23.16	0.726	24.78	0.775	23.86	0.745

The results of computational experiments prove a good scalability of the parallel algorithm. The decrease of the efficiency E_p for the largest case of test problems is explained by the influence of relatively slow network used to interconnect processors in Vilkas cluster. Thus in fact the bandwidth of the network β depends on the size of data transfered among processors. We also note that the nodes of the cluster are not fully homogeneous (the fluxtation of computational speed up till 8 percents was observed during experiments), therefore it is impossible to make a precise fitting of experimental results to a theoretical scaling estimate.

For real applications we solve the given problem for different values of parameters, in order to investigate the dependence of the quality of generated optical fields on various geometrical and constructive parameters. Thus it is important to estimate the CPU time required to solve one variant of the problem. As a real benchmark, we have solved on Vilkas cluster the discrete

problem of the size $M = 1080$, $2J = 1250$, the simulation was done till 5 ns. The required CPU time was 3441 seconds on the cluster with $36 = 9 \times 4$ cores.

8 Numerical Study of the Full TW Model

In this section we present a pair of numerical experiments solving full TW model (2.1), (2.2) in the spatial domain defined by $L = 4$ and truncation factor $X = 18$. To solve this problem we use numerical schemes (5.2)–(5.5). Following the observations of Section 6, we supplement these schemes with simple Dirichlet boundary conditions (5.1) for carrier densities and

$$E^{\pm,n}_{h,k,-J} = 0, \quad E^{\pm,n}_{h,k,J} = 0, \quad k = 0, \ldots, M, \quad n = 0, \ldots, K$$

for optical fields. We apply the discretization steps

$$h_z = 0.016/c', \quad h_{x,\pm|j-0.5|} = \frac{2X \sinh(0.75/\bar{J}c')}{c'(e^{1.5} - 1)} e^{1.5|j-0.5|/\bar{J}c'}, \quad |j - 0.5| < \bar{J}c' \tag{8.1}$$

with $\bar{J} = 187.5$ and $c' \in \{1, 2, 4, 6\}$. We note, that close to the lateral axis $z = 0$ these steps are in a good agreement with the uniform discretization steps (6.3) used in simulations of the auxiliary problem: compare $h_{x,\pm 0.5} \approx 0.041525$ with $h_x = 0.04$ while $h_z = 0.016$ and $c = c' = 1$.

Like in real experiments, we put our major attention to the simulation of the emitted field intensity $P(t) = \int |E^+(L, x, t)|^2 dx$ and the near field shape $|E^+(L, x, T)|^2$.

Amplification of the incoming optical beam. In this example we set parameters $\kappa^{\pm}(z, x) \equiv 0$, $r_0(x) \equiv -0.01$, $r_L(x) \equiv 0.01$, and an optical injection

$$a(x, t) = A_0 \exp\left(-\frac{(t - T_0)^2}{3.5^2} - \frac{x^2}{0.1} - 2ix\right) \quad \text{with} \quad A_0 = 30 \quad \text{and} \quad T_0 = 150.$$

In the physical dimensions $I(t) = \int |a(x, t)|^2 dx$ is a 50 ps long beam with $\sim$1W peak amplitude power.

Some representation of our simulations is given in Fig. 7. In this case our device is not able to generate optical field by itself, but works as an optical amplifier. For all considered grid steps the peak amplitude of the injected optical beam $I(t)$ was amplified by ≈ 100 times (see Fig. 7a). Moreover, in all cases the outgoing beam has a damped oscillating trailing edge, the shape of which, however, depends on the applied grid step.

It seems, that a main reason of these small differences is again a growing mismatch between the phases of the complex optical fields or between some intensity oscillations. This can be also recognized in Fig. 7(b) where a comparison of the lateral distributions of carrier functions $N(L, x, T)$ for different grid steps is made. While the mean profile and the oscillation period in all cases is reproduced similarly, the phases of these oscillations (which are induced by corresponding field intensity oscillations) differ.

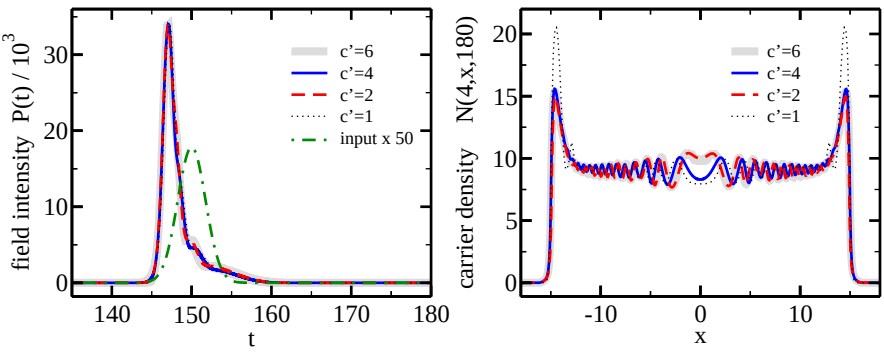

Figure 7. Amplification of the incoming optical beam. (a): time traces of the incoming beam $I(t)$ (dashed-dotted) and amplified field intensities $P(t)$ for the grid steps (8.1) with different c'. (b): corresponding profiles of carrier density $N(z, x, t)$ at $z = L$ and last time moment $T = 180$.

Generation of the optical field. In this case we set $a(x, t) \equiv 0$, $r_0(x) \equiv -0.04$, $r_L(x) \equiv 0.04$, and assume the presence of the Bragg grating within the narrow waveguide section S_1 by setting $\kappa^{\pm}(z, x) = 0.25\chi_1$. Due to significant field reflectivities at both edges of our device now it is able to generate the optical field.

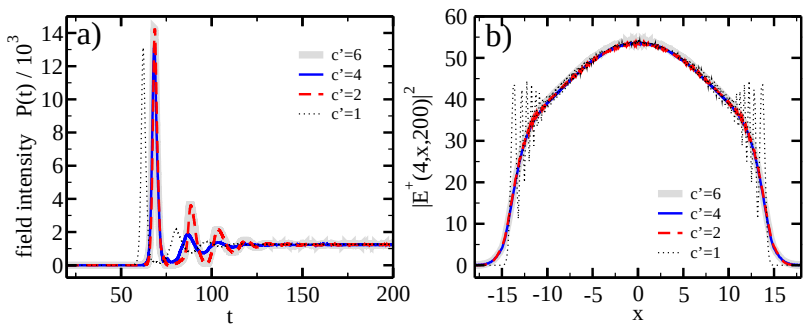

Figure 8. Switching on of the laser. (a): evolution of the emitted field intensity $P(t)$ for the grid steps (8.1) with different c'. (b): corresponding near fields $|E^+(z, x, t)|^2$ at the taper amplifier facet $z = L$ and last time moment $T = 200$.

Fig. 8 represents a switching on of the laser. Panel (a) shows typical time traces of the field intensity $P(t)$ during this switching process. Namely, after generation of the first large pulse we have a sequence of damped relaxation oscillations leading to some stable stationary (continuous wave) state. The emitted field intensity at this state as well as the *mean* profile of the near field $|E^+(L, x, T)|^2$ (Fig. 8 b) is similar for all applied grid steps.

However, comparing to the previously considered case, now we can much easier recognize numerical errors induced by sparse discretization steps (8.1) with $c' = 1$. They are represented by an earlier switching of the first pulse in panel (a) as well as by strongly oscillating flanks of the near field in panel

(b) of Fig. 8. In both cases we have seen that the emitted field *intensities* can be rather well reproduced by relatively sparse grid steps (8.1) with $c' = 1$. Thus, this discretization can be reasonable when performing simulations where only record of the mean field intensity is needed. However, once the precise resolution of the near fields, field phases, or complex dynamical regimes starts to be important one should choose some finer space and time discretization.

9 Conclusions

An effective parallel computing technique for simulation of dynamics in edge-emitting high power broad area semiconductor lasers and amplifiers was considered in this paper. This dynamics is described by the traveling-wave model which is a system of 1+2 dimensional partial differential equations defined in a laterally unbounded domain.

For optimization of the numerical grids and schemes for TW model we have also investigated a related 1+1 dimensional Schrödinger equation describing a diffractive beam propagation in linear gain and index guided media. By solving this auxiliary problem (3.1) in the broad enough domain with different types of lateral boundary conditions we have found, that BC induced errors have only a small impact to the precision of the numerical solutions: the effective absorption of the imperfect BC induced field radiation is provided by a smoothly with $|x| \to \infty$ decaying function $\Im m\mathcal{B}(z,x) < 0$. Moreover, we have found that the main source of numerical errors is a presence of narrow index-guiding regions characterized by sharp transitions of $\Re e\mathcal{B}(z,x)$ at certain values of lateral coordinate x. In order to keep these errors within the required limits one should use a fine lateral discretization of the neighborhood of these regions.

Acknowledgement

The work of M. Radziunas was supported by DFG Research Center MATHEON "Mathematics for key technologies: Modelling, simulation and optimization of the real world processes".

References

[1] X. Antoine, A. Arnold, Ch. Besse amd M. Ehrhardt and A. Schädle. A review of transparent and artificial boundary conditions techniques for linear and nonlinear Schrödinger equations. *Commun. in Comput. Physics*, **4**(4):729–796, 2008.

[2] S. Balsamo, F. Sartori and I. Montrosset. Dynamic beam propagation method for flared semiconductor power amplifiers. *IEEE Journal of Selected Topics in Quantum Electronics*, **2**:378–384, 1996. Doi:10.1109/2944.577398.

[3] U. Bandelow, M. Radziunas, J. Sieber and M. Wolfrum. Impact of gain dispersion on the spatio-temporal dynamics of multisection lasers. *IEEE J. Quantum Electron.*, **37**:183–188, 2001. Doi:10.1109/3.903067.

[4] P. Chazan, J.M. Mayor, S. Morgott, M. Mikulla, R. Kiefer, S. Müller, M. Walther, J. Braunstein and G. Weimann. High-power near difraction-limited tapered amplifiers at 1064 nm for optical intersatelite communications. *IEEE Phot. Techn. Lett.*, **10**(11):1542–1544, 1998. Doi:10.1109/68.726743.

[5] R. Čiegis, A. Jakušev and V. Starikovičius. Parallel tool for solution of multiphase flow problems. In N. Meyer R. Wyrzykowski, J. Dongarra and J. Wasniewski(Eds.), *Lecture notes in computer science. Sixth International conference on Parallel Processing and Applied Mathematics. Poznan, Poland, September 10–14, 2005*, volume 3911, pp. 312–319, Berlin, Heidelberg, New York, 2006. Springer. Doi:10.1109/68.726743.

[6] R. Čiegis, I. Laukaitytė and M. Radziunas. Numerical algorithms for Schrödinger equations with absor bing boundary conditions. *Nonlinear Functional Analysis and Optimization*, **30**(9-10):903–923, 2009. Doi:10.1080/01630560903393097.

[7] R. Čiegis, M. Radziunas and M. Lichtner. Numerical algorithms for simulation of multisection lasers by using traveling wave model. *Math. Model. Anal.*, **13**(3):327–348, 2008. (Doi:10.3846/1392-6292.2008.13.327-348)

[8] A. Egan, C. Z. Ning, J. V. Moloney, R. A. Indik, M. W. Wright, D. J. Bossert and J. G. McInerney. Dynamic instabilities in master oscillator power amplifier semiconductor lasers. *IEEE J. Quantum Electron.*, **34**(1):166–170, 1998. Doi:10.1109/3.655020.

[9] I. Laukaitytė, R. Čiegis, M. Lichtner and M. Radziunas. Parallel numerical algorithm for the traveling wave model. In R. Ciegis, D. Henty, B. Kagstrōm and J. Žilinskas(Eds.), *Parallel Linear Algebra and Optimization: Advances and Applications. Springer Optimization and Its Applications. ISBN: 978-0-387-09706-0*, volume 27, pp. 237–250, New-York, 2009. Springer.

[10] M. Maiwald, S. Schwertfeger, R. Güther, B. Sumpf, K.Paschke, C. Dzionk, G. Erbert and G. Tränkle. 600 mW optical output power at 488 nm by use of a high-power hybrid laser diode system and a periodically poled Mgo:LiNbo$_3$. *Optics Letters*, **31**(6):802–804, 2006. Doi:10.1364/OL.31.000802.

[11] M. Pessa, J. Näppi, P. Savolainen, M. Toivonen, R. Murison, A. Ovchinnikov and H. Asonen. State-of-the-art aluminum-free 980-nm laser diodes. *J. Ligthw. Technol.*, **14**(10):2356–2361, 1996. Doi:10.1109/50.541229.

[12] W. Schultz and R. Poprawe. Manufacturing with nover high-power diode lasers. *IEEE J. Select. Topics Quantum Electron.*, **6**(4):696–705, 2000. Doi:10.1109/2944.883386.

[13] M. Spreemann, M. Lichtner, M. Radziunas, U. Bandelow and H. Wenzel. Measurement and simulation of distributed-feedback tapered master-oscillators power-amplifiers. *IEEE J. of Quantum Electron.*, **45**(6):609–616, 2009. Doi:10.1109/JQE.2009.2013115.

[14] J. Szeftel. Design of absorbing boundary conditions for Schrödinger equation in R^d. *SIAM J. Numer. Anal.*, **42**(4):1527–1551, 2004. Doi:10.1137/S0036142902418345.